Check for updates

A fluorescent nanohybrid sensor based on carbon dots encapsulated in a metal organic framework for highly selective and sensitive detection of mercury

Imtiyaz Ahmad Lone and Jigneshkumar V. Rohit (ID) *

The accurate and sensitive detection of toxic heavy metals, particularly mercury ions, in aquatic environments is crucial due to their severe environmental persistence and detrimental health effects. In this study, we report the synthesis and application of a novel fluorescent sensor based on carbon dots encapsulated within a zeolitic imidazolate framework (CDs@ZIF-8) for the selective and sensitive detection of Hg^{2+} in aqueous media. The carbon dots were synthesized *via* a hydrothermal method using *m*-phenylenediamine and L-ascorbic acid, followed by *in situ* encapsulation into the ZIF-8 matrix through a one-pot solvothermal strategy. Structural and morphological characterization confirmed the successful formation and integration of CDs within the ZIF-8 framework without compromising its crystallinity or thermal stability. The resulting CDs@ZIF-8 sensor exhibited strong blue fluorescence with excellent photostability, environmental tolerance, and dispersibility in water. Notably, the sensor demonstrated high sensitivity toward Hg^{2+} ions, with a wide linear detection range of 0.01–1.0 μM, having a low detection limit of 83 nM and a quenching constant of 6.17 $\times 10^6$ M^{-1}. The fluorescence quenching followed a concentration-dependent Stern–Volmer relationship and was visually detectable under UV light. Real water sample analysis revealed recovery rates between 95.54% and 99.01%, confirming the practical applicability of the sensor. These findings suggest that the CDs@ZIF-8 platform holds significant promise as a cost-effective, portable, and environmentally friendly fluorescent probe for real-time Hg^{2+} monitoring in environmental samples.

1. Introduction

Mercury (Hg^{2+}), a highly toxic heavy metal, presents substantial environmental and health hazards due to its bioaccumulation, persistence, and potent toxicity at even trace levels.[1] It is commonly released into the environment through industrial activities such as coal combustion, mining, and certain manufacturing processes, as well as through natural phenomena like volcanic eruptions.[2] Once in the environment, Hg^{2+} undergoes chemical transformations, leading to the formation of toxic species such as methylmercury, which can bio-accumulate in aquatic organisms and magnify through the food chain.[3] This process ultimately leads to Hg^{2+} presence in human diets, especially through seafood consumption, creating serious health concerns, including neurological damage, kidney dysfunction, and developmental disorders.[4,5] Instrumental methods for detecting Hg^{2+} in environmental and biological samples rely on advanced analytical techniques such as high-performance liquid chromatography (HPLC),[6] inductively coupled plasma mass spectrometry (ICP-MS),[7] and atomic absorption spectroscopy (AAS).[8] While these methods offer high sensitivity and accuracy, they typically require costly equipment, intricate sample preparation, and skilled operators, limiting their practicality for rapid or in-field testing.[9] Fluorescence-based sensors have gained prominence as a highly effective approach for mercury detection, owing to their exceptional sensitivity, fast response times, and the potential for miniaturization and portable applications, making them ideal for real-time monitoring.[10,11] These sensors operate by detecting changes in fluorescence properties upon interaction with mercury ions, providing a straightforward and fast method for quantifying mercury concentrations. Among the innovative approaches in this domain, carbon dot encapsulated metal–organic frameworks (CDs@MOFs) have emerged as a groundbreaking advancement in the field, celebrated for their remarkable versatility and tunable properties.[12,13]

Fluorescent carbon dots (CDs) are a new class of quantum-sized luminescent nanoparticles that have gained significant attention due to their exceptional optical characteristics and

Department of Chemistry, National Institute of Technology Srinagar - 190006, Jammu and Kashmir, India. E-mail: jignesh@nitsri.ac.in, jvrsvnit@gmail.com; Tel: +91 9909500225

promising applications.[14] In comparison to traditional organic dyes, metallic quantum dots, and other phosphor-based materials, CDs offer several notable benefits, including strong fluorescence emission, simple and eco-friendly synthesis routes, low toxicity, and outstanding stability in aqueous environments.[15,16] Compared to conventional fluorescent materials, CDs exhibit distinctive features such as superior water solubility, high photoluminescence quantum yield, and remarkable resistance to photobleaching.[17] Additionally, their surfaces are enriched with abundant functional groups, including carboxyl, hydroxyl, and amino moieties.[18,19] These surface functionalities enable CDs to interact with various metal ions, facilitating charge transfer processes between the metal ions and the CDs. Such interactions can subsequently lead to fluorescence quenching of the CDs.[20] Despite these advantages, the aggregation caused quenching (ACQ) effect poses a challenge, similar to conventional fluorescent dyes.[21] At low concentrations, CDs are uniformly dispersed, but as the concentration increases, significant aggregation occurs, hindering their applications.[22] Overcoming the ACQ effect requires addressing the inevitable problem of preventing CD accumulation.[23] Combating this challenge is a crucial research direction.

One effective approach involves the incorporation of fluorescent CDs into composite materials. Therefore, selecting and developing suitable host materials represents a significant and effective strategy to expand the applications of CDs. As a result, CD encapsulated composites have become highly promising fluorescent materials, finding extensive use in the development of various fluorescent probes and sensors. Porous materials have been recognized as excellent candidates for hosting functional nano CDs, primarily attributed to the unique nanometer-scale confined spaces within these materials.[24,25] Concurrently, CDs possess nanoscale dimensions and abundant surface functional groups, making them well-suited for integration with porous materials to create composite materials. Currently, a variety of porous materials, including zeolites,[26,27] metal–organic frameworks (MOFs),[28,29] mesoporous materials[30,31] and other porous nanocarriers,[32] are being employed as host materials for this purpose. Among multitudinous porous materials, MOFs are crystalline structures composed of metal ions or clusters coordinated with organic linkers, forming highly ordered, porous networks.[33–35] Compared to traditional inorganic and porous carbon materials, MOFs provide several key advantages like a precisely defined crystalline structure, enabling detailed insights into their architectural features; high porosity and large specific surface area; structural versatility and tunability; intrinsic flexibility; and ease of chemical modification or functionalization.[36,37] These attributes position MOFs for potential applications across various fields, including gas adsorption and separation, catalysis, proton conductors, luminescence, and sensing.[38,39]

Zeolitic imidazolate frameworks (ZIFs), a notable subclass of MOFs, are formed by the coordination of metal ions with organic imidazolate ligands, producing zeolite-like structures with a supramolecular microporous network.[40] Among various ZIFs, ZIF-8 has attracted considerable attention due to its advantageous properties, including facile synthesis, water dispersibility, and outstanding chemical and thermal stability,[41,42] and exceptional stability.[43] Capitalizing on the porous architecture of ZIF-8, it functions as an optimal host matrix for the encapsulation of CDs. This approach mitigates fluorescence quenching due to aggregation and promotes the effective capture and concentration of analytes. In this study, we present a simple yet effective approach to immobilize CDs within the channels of ZIF-8, resulting in the development of a highly luminescent CDs@ZIF-8 sensor. Fluorescent CDs were synthesized *via* a hydrothermal method and subsequently incorporated into the ZIF-8 framework through a one-pot *in situ* modification strategy (as illustrated in Scheme 1). This hybrid material harnesses the superior adsorption capacity of ZIF-8 and integrates it with the remarkable optical properties of CDs. Real-time fluorescence studies revealed that the addition of Hg^{2+} ions significantly quenched the fluorescence of the CDs@ZIF-8, producing a distinct and observable color change under UV light. Moreover, the sensor was capable of detecting the presence of Hg^{2+} in various water samples (lake, river and tap water). These findings, highlights the potential of CDs@ZIF-8 as a reliable, efficient, and visually perceptive tool for Hg^{2+} sensing in environmental water samples.
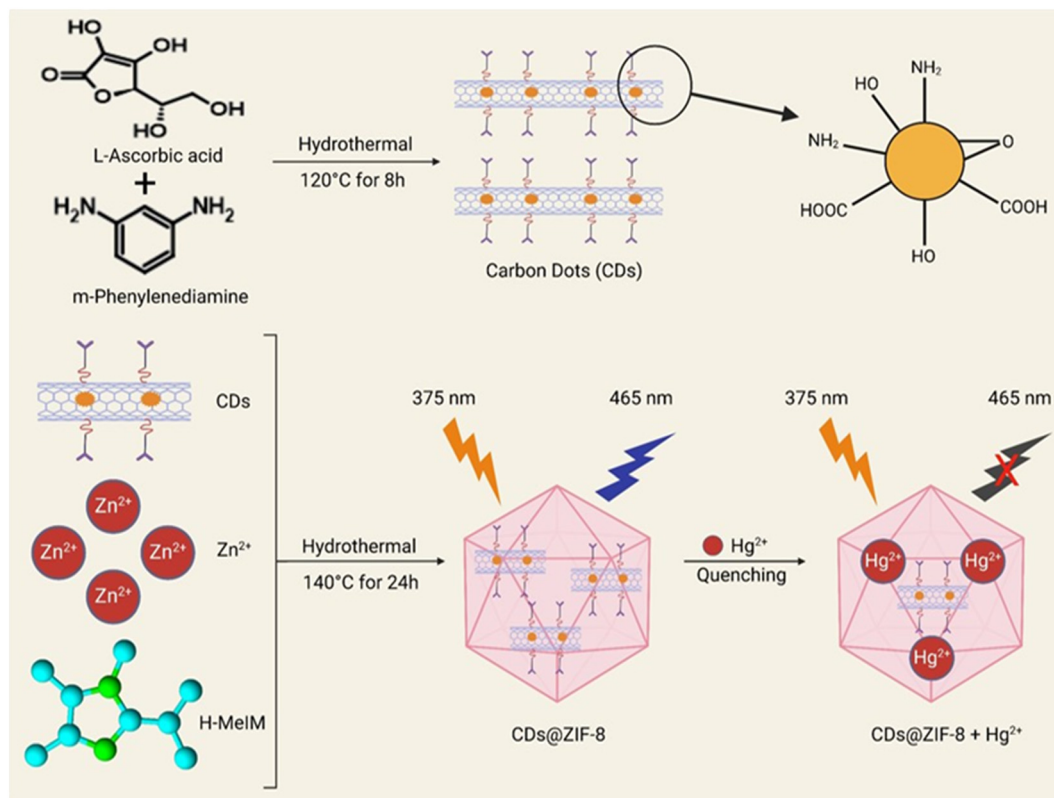
2. Materials and methods

2.1. Materials and reagents

All reagents and chemicals utilized in this work were of analytical grade and used as received without further purification. Zinc nitrate hexahydrate $(Zn(NO_3)_2 \cdot 6H_2O)$, 2-methylimidazole (H-MeIM), *m*-phenylenediamine (*m*-PD), and L-ascorbic acid (L-AA) were obtained from Sigma-Aldrich Chemicals Co. Stock aqueous solutions of Zn^{2+}, Ni^{2+}, Na^+, Mg^{2+}, K^+, Pb^{2+}, Cu^{2+}, Ca^{2+}, Al^{3+}, Ag^+, Ba^{2+}, Cd^{2+}, Mn^{2+}, and Co^{2+} were freshly prepared from their respective nitrate salts. Organic solvents, including hexane, methanol (MeOH), *N,N'*-dimethylformamide (DMF), ethanol (EtOH), acetone, toluene, and dimethyl sulfoxide (DMSO), as well as dialysis membranes (molecular weight cut-off: 1000 Da), were purchased from Sigma-Aldrich. Ultrapure water was supplied by an aquaMAX Ultra 370 purification system.

2.2. Material characterization

The structural formation of the prepared material has been investigated by recording its X-ray diffraction (XRD) pattern using a Bruker-D8 advance diffractometer using a Cu-target (= 1.5406 Å) irradiation in the range of 5–70°. The Fourier transform infrared (FTIR) spectrum was recorded using KBr pellets on a Perkin Elmer (FTIR-2000, USA) spectrometer to identify functional groups. To evaluate the optical properties, fluorescence emission spectra were recorded at 25 ± 0.1 °C using a Cary Eclipse Fluorescence 15 spectrophotometer (Cary 100, Agilent, USA). The surface morphology and microstructural features were

Scheme 1 Schematic representation of the preparation of luminescent CDs@ZIF-8 hybrid nano-sensor and its application as a fluorescent sensor for Hg^{2+} detection.

investigated by scanning electron microscopy using a JEOL Model JSM-6390LV (Japan Electron Optics Laboratory Co., Ltd., Japan). Thermogravimetric analysis (TGA) was conducted on a Perkin–Elmer SSC-5200 TG-DTA (USA) analyzer to assess thermal stability. Additionally, specific surface area and pore characteristics were determined by measuring N_2 adsorption/desorption isotherms at 77 K using a Quantachrome ASiQwin v5.2 surface area analyzer (USA). Transmission electron microscopy analysis was performed using an FEI Titan electron microscope (Japan) operating at 80 kV.

2.3. Preparation of carbon dots

CDs were prepared following an optimized adaptation of a one-pot hydrothermal synthesis method previously reported in the literature.[44,45] The procedure commenced with the precise weighing of 460.0 mg of L-AA and 210.0 mg of *m*-PD, followed by dissolution in 10.0 mL of ultrapure water. The resulting mixture was carefully transferred into a Teflon-lined stainless steel autoclave and subjected to hydrothermal treatment at 120 °C (±2 °C) for 8 hours. Upon completion of the reaction, the system was allowed to naturally cool to room temperature. The solution was then purified by centrifugation at 12000 rpm for 15 minutes to separate any residual solids. The resulting supernatant was filtered through a 0.22 μm membrane and further purified by dialysis against ultrapure water for 24 hours, utilizing a dialysis bag

with a molecular weight cutoff of 1000 Da. This process yielded a suspension of CDs. To preserve the CDs for later use, the suspension was stored in a dark place at a temperature of 4 degrees Celsius (±0.5 degrees). It's worth noting that the starting materials for this process are non-toxic and environmentally friendly.

2.4. Preparation of CDs@ZIF-8

The *in situ* synthesis of CDs@ZIF-8 was carried out *via* the hydrothermal method, following the protocol outlined by Venna *et al.*[46] Initially, 8.0 mmol of H-MeIM was dissolved in 15 mL of DMF, after which 50 μL of the CD solution was added to the mixture. In a separate container, $Zn(NO_3)_2 \cdot 6H_2O$ (1.0 mmol) was dissolved in 15 mL of DMF. The $Zn(NO_3)_2 \cdot 6H_2O$ solution was then swiftly poured into the H-MeIM solution and stirred vigorously for 1 hour at room temperature. The mixture was then heated at 140 °C for 24 hours in a hydrothermal reactor. The sensor was thoroughly washed several times with DMF and deionized water, followed by drying under vacuum at 60 °C for 6 hours to obtain the final product.

2.5. Pretreatment of real water samples

Tap water was collected from the laboratory, Department of Chemistry, National Institute of Technology Srinagar, Jammu and Kashmir, India; the river water from the Jhelum River of

the Srinagar municipal area, Jammu and Kashmir, India; the lake water from the Dal Lake of Srinagar municipal area, Jammu and Kashmir, India. All samples were first filtered through a 0.45 micron filter to remove suspended particulate matter. The standard addition method was used to spike the water samples. The filtered samples were spiked with known concentrations of Hg^{2+} ions to evaluate the performance of the CDs@ZIF-8 sensor under realistic conditions. The spiking procedure involved adding appropriate volumes of a standard Hg^{2+} solution to achieve the desired concentrations, followed by gentle mixing to ensure homogeneity. The prepared samples were then subjected to fluorescence measurements.

3. Results and discussion

3.1. Characterization of the CDs@ZIF-8 based optical sensor

To verify the successful synthesis of CDs@ZIF-8, the material was characterized using PXRD and FT-IR. The PXRD pattern of the synthesized ZIF-8 (Fig. 1) exhibits intense diffraction peaks at 2θ values of 7.30°, 10.35°, 12.70°, 14.80°, 16.40°, and 18.00°, which are indexed to the (110), (200), (211), (220), (310), and (222) crystal planes, respectively. The sharpness and intensity of these reflections confirm the formation of a highly crystalline ZIF-8 framework. The modified ZIF-8 exhibited diffraction peaks identical to those of pristine ZIF-8, indicating that the crystal structure was preserved and remained intact despite the introduced modifications, confirming that the integration of CDs had no effect on the topological framework of ZIF-8.

FT-IR analysis was employed to provide deeper insights into the successful formation of CDs@ZIF-8. A similar pattern was observed in the FT-IR spectra, where the characteristic absorption peaks of both ZIF-8 and CDs@ZIF-8 aligned with those reported in previous studies.[47] The FTIR spectrum of the synthesized CDs exhibits a broad absorption band around 3400 cm^{-1}, which is attributed to the stretching
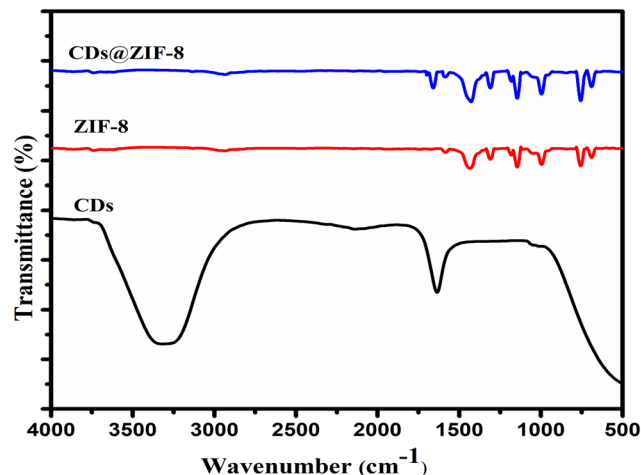

Fig. 2 FT-IR spectra of CDs, ZIF-8, and CDs@ZIF-8.

vibrations of hydroxyl (–OH) or amine (–NH) functional groups (Fig. 2). A prominent peak observed near 1700 cm^{-1} corresponds to the C=O stretching vibration, indicating the presence of carbonyl or carboxylic groups. Peaks in the range of 1500–1300 cm^{-1} are associated with C=C and C–N stretching vibrations, suggesting aromatic and/or amine functionalities. Additionally, characteristic bands appearing in the 1100–1000 cm^{-1} region are ascribed to C–O or C–O–C stretching, which are typically observed in alcohols or ethers. These spectral features collectively confirm the successful synthesis of CDs. In the spectrum (red line) the synthesized material displays absorption bands in the range of 3130–2950 cm^{-1}, which are attributed to C–H stretching vibrations characteristic of the imidazole ring. A distinct peak observed at 1580 cm^{-1} corresponds to C=N stretching, while the bands appearing between 1350 and 1100 cm^{-1} are assigned to C–N stretching vibrations, further confirming the presence of imidazole-based linkers. Additionally, peaks in the range of 760–690 cm^{-1} are indicative of Zn–N coordination bonds, providing strong evidence for the successful formation of the ZIF-8 framework. And in the CDs@ZIF-8 spectrum (blue line), all the characteristic peaks of ZIF-8 confirm that the MOF structure is retained. Additional broadness near 3400 cm^{-1} and a weak band around 1700 cm^{-1} indicate the presence of CDs (O–H, N–H, and C=O groups). Slight peak shifts or intensity changes in the 1400–1000 cm^{-1} region suggest interactions between CDs and the ZIF-8 framework. These spectral changes confirm the successful encapsulation of CDs into ZIF-8.

TGA was conducted to evaluate the thermal stability of the synthesized sensor. As depicted in Fig. S1, which illustrates the weight change with increasing temperature, the decomposition temperature of CDs@ZIF-8 was observed to be approximately 580 °C. The observed weight loss in the 200–500 °C range was ascribed to the evaporation of trapped solvents and the thermal degradation of amide groups present in the CDs. Beyond 580 °C, the weight loss was associated with the collapse of the ZIF-8 framework. From
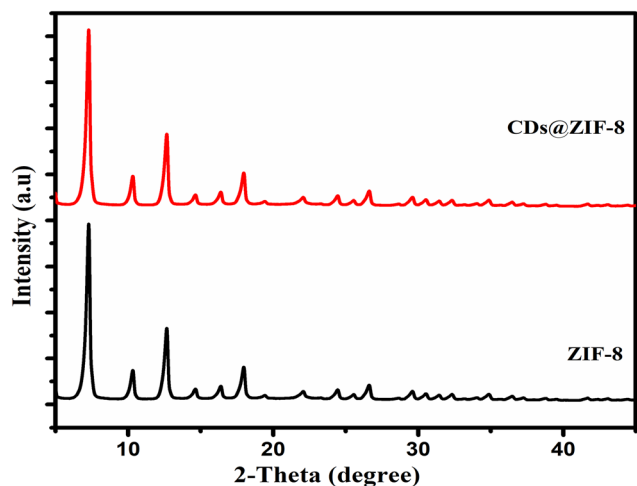

Fig. 1 XRD patterns of synthesized pristine ZIF-8, and the fluorescent probe sensor (CDs@ZIF-8).

the TGA data, it was estimated that the CDs constituted approximately 0.74 wt% of the total weight, indicating successful encapsulation within the ZIF-8 pores. The superior thermal stability of the CDs@ZIF-8 hybrid can be ascribed to the synergistic interaction between the CDs and the MOF, further validating the effective immobilization of CDs within the MOF.[48,49] When the CD concentration increased, the fluorescence intensity increases but the XRD peaks of ZIF-8 (10–30° 2θ) decreased in intensity and broadened slightly, indicating partial lattice distortion and the amorphous contribution of excess CDs, while still retaining the crystalline framework (Fig. S2). Notably, the decomposition temperature and overall trend of CDs@ZIF-8 closely mirrored that of pristine ZIF-8, suggesting that the encapsulation of CDs did not compromise the structural integrity or thermal stability of the MOF. To analyze its surface and morphological features, the synthesized nanosensor was characterized by SEM, where the results revealed that

CDs@ZIF-8 exhibited a well-defined polyhedral shape, as depicted in Fig. 3b. This observation aligns with the crystalline morphology of ZIF-8 (Fig. 3a) and those previously documented in the literature.[50] This confirms the structural integrity and successful synthesis of the hybrid material. The morphology of the as-synthesized CDs was further investigated using TEM, and the image is presented in Fig. S3. The CDs appeared as uniformly dispersed quasi-spherical nanoparticles with an average particle size of 7.0 nm. Elemental analysis of CDs@ZIF-8 was conducted to identify the elements present in the samples. The EDS spectrum of CDs@ZIF-8 (Fig. 3c) displayed the Kα peaks corresponding to Zn, C, O, and N. No additional peaks corresponding to foreign elements were detected, indicating the high purity of the material. Also there is an O peak in the spectrum which successfully confirms the encapsulation of CDs. On the other hand, elemental mapping confirms the homogeneous dispersion of Zn, C, O, and N in the selected area of the
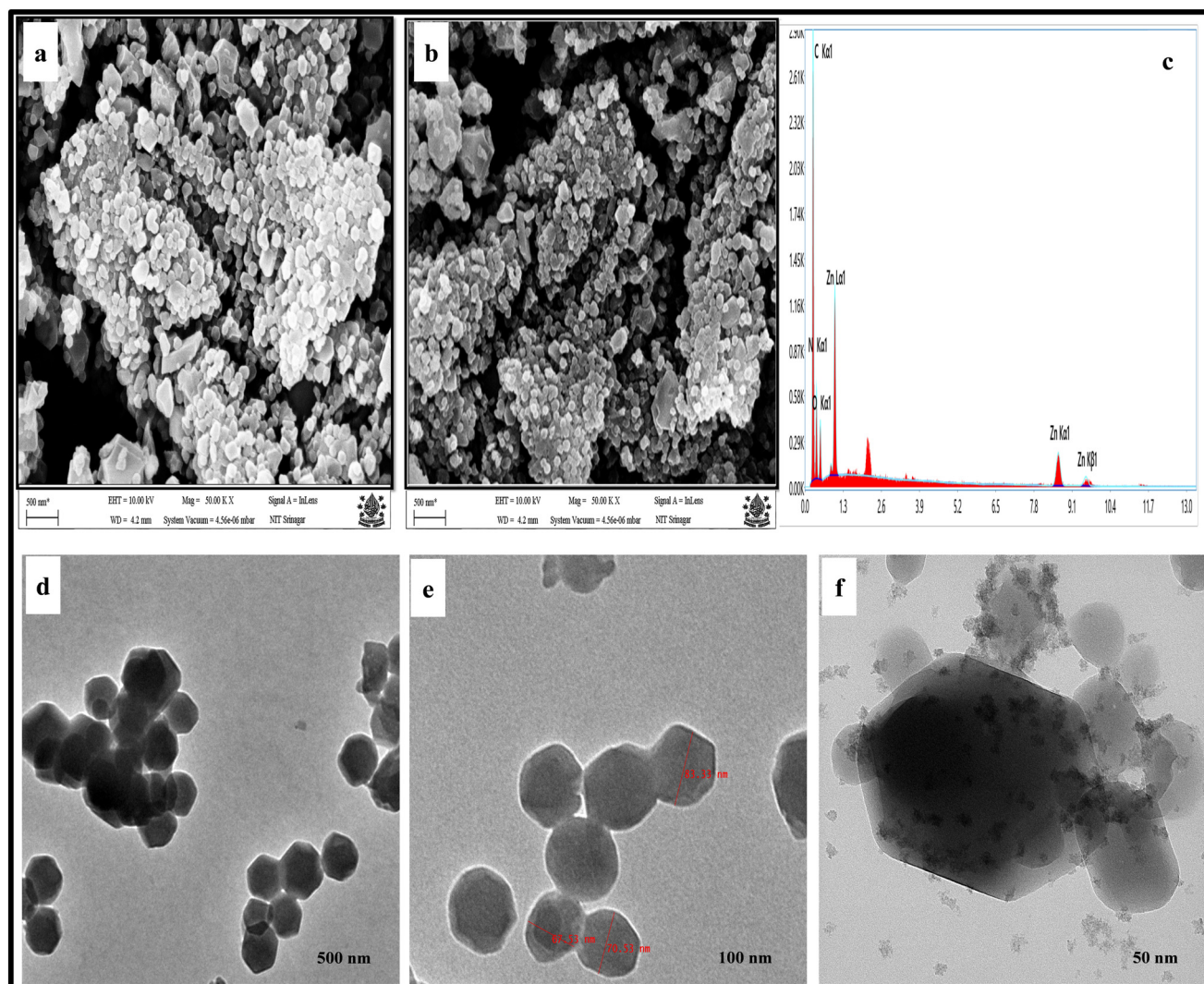

Fig. 3 SEM images of (a) ZIF-8 at a scale of 500 nm and (b) CDs@ZIF-8 at a scale of 500 nm. EDS spectra of (c) CDs@ZIF-8. TEM images of CDs@ZIF-8 (d) at a scale of 500 nm, (e) at a scale of 100 nm, and (f) at a scale of 50 nm.

CDs@ZIF-8 (Fig. S4). The weight percentage of existing elements in the samples is presented in Table S1. The spectrum shows 58.5% wt of C, 24% wt of N, 9.2% wt of O and 7.6% wt of Zn. The high carbon and nitrogen contribute to the linker 2MeIM and the CDs. And TEM images (Fig. 3d–f) at different resolutions also reveal that the as-prepared CDs@ ZIF-8 sensor particles exhibit a rhombic dodecahedral structure with an average size of approximately 70 nm. Meanwhile, the results of TEM were consistent with the SEM results. The above phenomenon preliminarily proved that the CDs@ZIF-8 was successfully synthesized. As illustrated in Fig. S5, the nitrogen adsorption–desorption isotherms reveal that the specific surface area of pristine ZIF-8 is 1988.964 m^2 g^{-1}. In comparison, the specific surface area of the CDs@ZIF-8 sensor is slightly reduced to 1929.839 m^2 g^{-1}. This reduction indicates the successful encapsulation of CDs within the ZIF-8 channels. Notably, both ZIF-8 and CDs@ZIF-8 exhibit the same type of adsorption–desorption isotherm, confirming that the skeletal structure of ZIF-8 remains intact following the incorporation of CDs. This result underscores the effective synthesis of the nanosenor without compromising the frameworks' structural integrity.

3.2. Luminescence behavior of the CDs@ZIF-8 sensor

To comprehensively study the fluorescence characteristics of the CDs@ZIF-8 sensor, the emission spectra of aqueous solutions of CDs, ZIF-8, and CDs@ZIF-8 were measured using an excitation wavelength of 375 nm. As illustrated in Fig. 4, the CDs@ZIF-8 exhibits a prominent fluorescence emission peak at approximately 465 nm, which almost coincides with the fluorescence spectra of CDs, whereas pure ZIF-8 shows no discernible emission peak.

This clearly indicates that the observed blue fluorescence (image on the right side of the inset in Fig. 4) of the CDs@ZIF-8 sensor is attributed to the CDs rather than ZIF-8, and the incorporation of CDs into ZIF-8 does not compromise their fluorescence properties, and the sensor exhibits a milky-white appearance under natural light (image on the left side of the

Fig. 4 Fluorescence emission spectra of CDs, ZIF-8, and CDs@ZIF-8. Images of CDs@ZIF-8 dispersed in ethanol under visible light (left) and 365 nm UV illumination (right).

inset in Fig. 4). Furthermore, the fluorescence emission spectra of CDs@ZIF-8 were examined across various excitation wavelengths (300, 320, 340, 375, 390, 410, 430, and 470 nm). The corresponding CIE chromaticity diagram illustrates the emission color coordinates derived from the photoluminescence spectra using the CIE 1931 framework. As shown in the diagram (Fig. S6), an increase in excitation wavelength from 350 to 400 nm results in predominantly blue emission. Further excitation from 400 to 470 nm leads to a gradual shift toward green emission. This progressive transition in emission color confirms the tunable luminescence properties of the sensor, which are strongly dependent on the excitation wavelength. The maximum fluorescence intensity of CDs@ZIF-8 was observed at an excitation wavelength of 375 nm.

To further validate the potential of CDs@ZIF-8 as a reliable fluorescent probe, we dispersed the composite powder in aqueous solutions under diverse conditions and meticulously assessed its fluorescence stability in both routine and extreme environments. Initially, a pure aqueous solution of the composite was prepared and monitored over a week, as depicted in (Fig. 5a). Daily fluorescence measurements revealed that the composite maintained a consistent intensity throughout the observation period, indicating exceptional stability and making it highly suitable for long-term applications in fluorescence sensing systems. Following this, we investigated the influence of varying pH (2–12) conditions on the fluorescence behavior of the composite, and in a wide salt concentration range of 0.2–1.0 M as shown in (Fig. 5b and c). While minor reductions in fluorescence intensity were detected under highly alkaline conditions, the decrease was negligible, demonstrating the material's resilience across a wide pH range. The different pH of the sensor was maintained using 1.0 M HCl and NaOH solutions. Furthermore, the fluorescence intensity remained robust under neutral conditions, which are commonly encountered in practical applications. These results highlight the remarkable stability of CDs@ZIF-8, both in terms of temporal consistency and environmental tolerance. This durability, coupled with its ability to withstand challenging conditions such as pH extremes, positions the composite as a highly reliable and versatile candidate for constructing advanced fluorescence sensing platforms. Additionally, the resistance to environmental interference reinforces its potential for deployment in real-world analytical applications, including environmental monitoring and chemical sensing.

3.3. Fluorescence sensing of Hg^{2+}

The impact of various organic solvents on the luminescent intensity of the composite was systematically investigated. Among the tested solvents, the composite exhibited strong fluorescence in methanol, ethanol, and DMSO, as illustrated in Fig. S7. Considering both the excellent dispersibility and the environmentally friendly nature of ethanol, it was selected as the optimal solvent for subsequent testing. The remarkable fluorescence properties of the composites prompted an in-depth investigation into their potential for
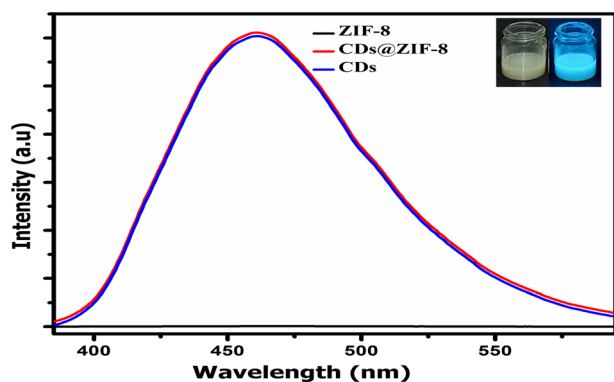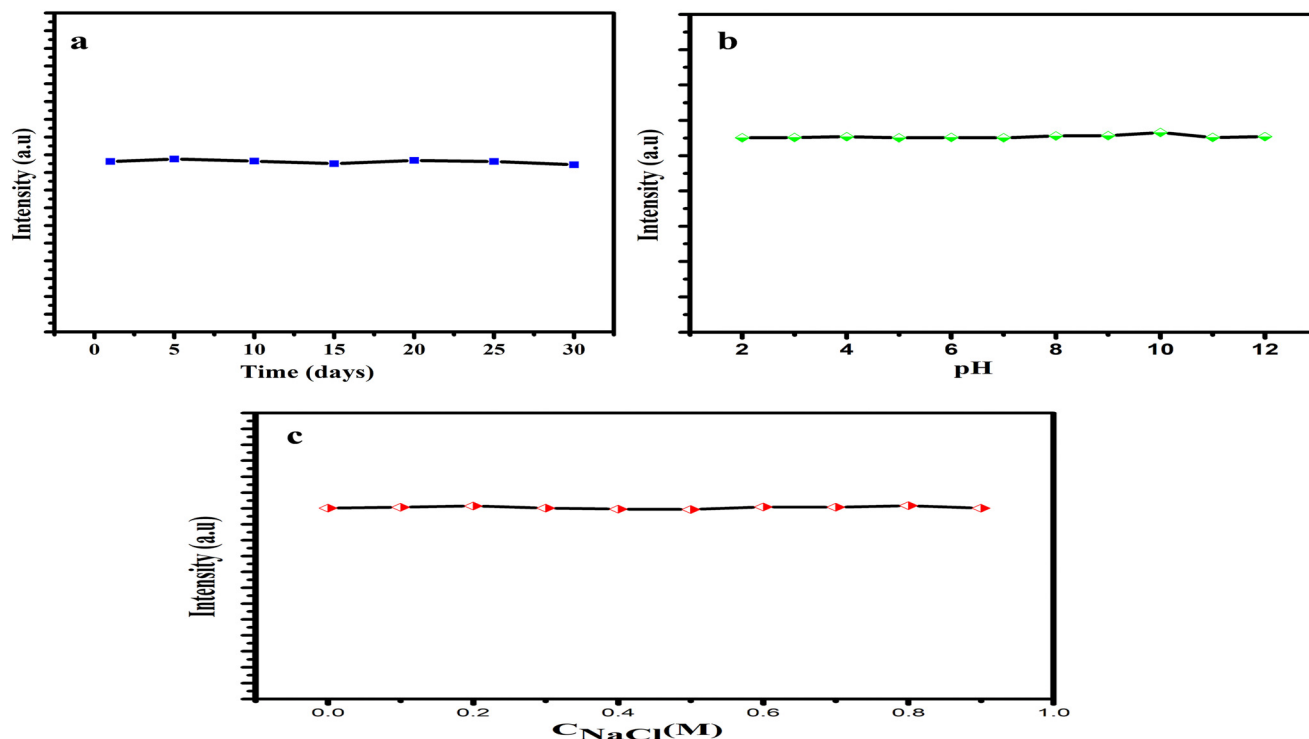
Fig. 5 (a) The FL intensities of CDs@ZIF-8 of different storage days (b) at different pH values and (c) in different concentrations of NaCl.

metal ion sensing applications. To determine their selectivity, a variety of metal ions were individually introduced into the fluorescence sensing solution, and the corresponding

emission spectra were meticulously recorded. As depicted in Fig. 6a, the composites exhibited distinct fluorescence responses to each metal ion, with most causing minimal
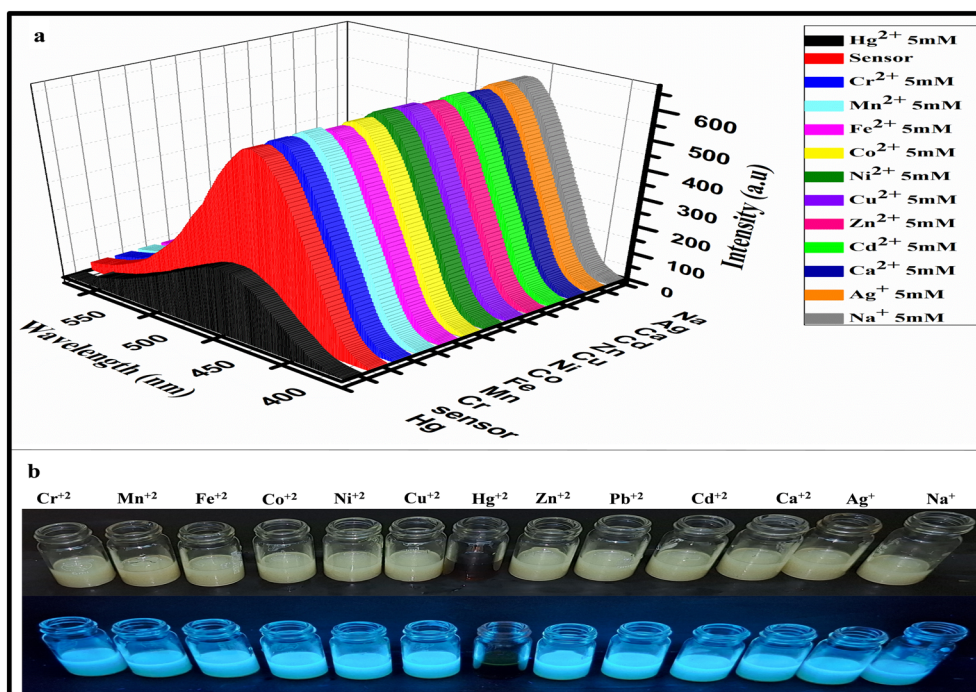

Fig. 6 (a) Comparative fluorescence intensities of CDs@ZIF-8 in the presence of various metal ions at an excitation wavelength of 375 nm, demonstrating selective response behavior. (b) The fluorescence images of the sensor both prior to and following the detection of Hg^{2+} ions are captured under a UV lamp.

changes or inducing a slight quenching effect. However, Hg^{2+} ions demonstrated a strikingly different behavior, producing a significant quenching of the fluorescence intensity. This drastic reduction in fluorescence upon the addition of Hg^{2+} clearly sets it apart from other tested ions, showcasing its unique interaction with the composites.

The fluorescence intensity before and after the introduction of Hg^{2+} showed a pronounced contrast, emphasizing the high sensitivity of the composites toward Hg^{2+} detection. This distinct behavior is attributed to the strong interaction between Hg^{2+} ions and the functional groups within the composite structure, which likely facilitates energy transfer or electron exchange mechanisms, leading to fluorescence quenching. These results confirm that the composites are not only selective but also highly efficient for the fluorescence-based detection of Hg^{2+} ions. Their simplicity, reliability, and high sensitivity position them as promising candidates for use in environmental monitoring. Fig. 6b illustrates the fluorescence images of the composites both prior to and following the detection of Hg^{2+} ions. The images, captured under a UV lamp, visually highlight the dramatic change in fluorescence. It is evident that Hg^{2+} induces a significant quenching effect on the composites, offering a striking visual and spectral confirmation of its strong interaction with the material. There is no such effect of sensing of Hg^{2+} with pure CDs, which is further confirmed under a UV lamp as shown in Fig. S8.

The ability to resist interference is a critical aspect in assessing the fluorescence sensing capabilities of materials. To evaluate this property, the composites were tested by sequentially introducing various interfering ions into the sensing solution containing Hg^{2+}, with the concentration of interfering ions set at ten times that of Hg^{2+}.[51] Changes in fluorescence intensity were carefully monitored to assess the

composites' anti-interference performance, highlighting their robustness and reliability as sensing materials. As illustrated in Fig. 7, the sensing solutions containing Hg^{2+} maintained a consistent quenching level, even after the introduction of various other metal ions. This stability demonstrates the remarkable anti-interference capability of the composites, highlighting their potential for the specific and reliable detection of Hg^{2+} without being influenced by competing ions.

Fluorescence titration experiments were conducted to explore the influence of varying concentrations of Hg^{2+} in aqueous solution on the fluorescence intensity of CDs@ZIF-8. As illustrated in Fig. 8a, the fluorescence intensity of CDs@ZIF-8 at 465 nm exhibited a progressive decline as the concentration of mercury ions increased from 0.01 to 1.0 μM. This steady decrease continued until the titration reached its endpoint, demonstrating a clear concentration-dependent quenching effect of Hg^{2+} on the fluorescence of CDs@ZIF-8. Fig. 8b illustrates the relationship between the relative fluorescence intensity (F_0/F) of the CDs@ZIF-8 sensing solution and varying concentrations of Hg^{2+}. The data reveal a nonlinear trend in relative fluorescence intensity across the full concentration range of 0.01–1.0 μM. However, within the narrower range of 0–1.0 μM, the composite demonstrates a strong linear correlation between fluorescence intensity and Hg^{2+} concentration. This observation highlights the sensor's advantage of offering a broad and reliable linear range for Hg^{2+} detection, making it highly effective for practical sensing applications.

The fluorescence quenching behavior of CDs@ZIF-8 aligns with the Stern–Volmer equation: $F_0/F = K_{sv}[M] + 1$, where F_0/F denotes the fluorescence intensities before and after the detection of Hg^{2+}. [M] denotes the Hg^{2+} concentration, and
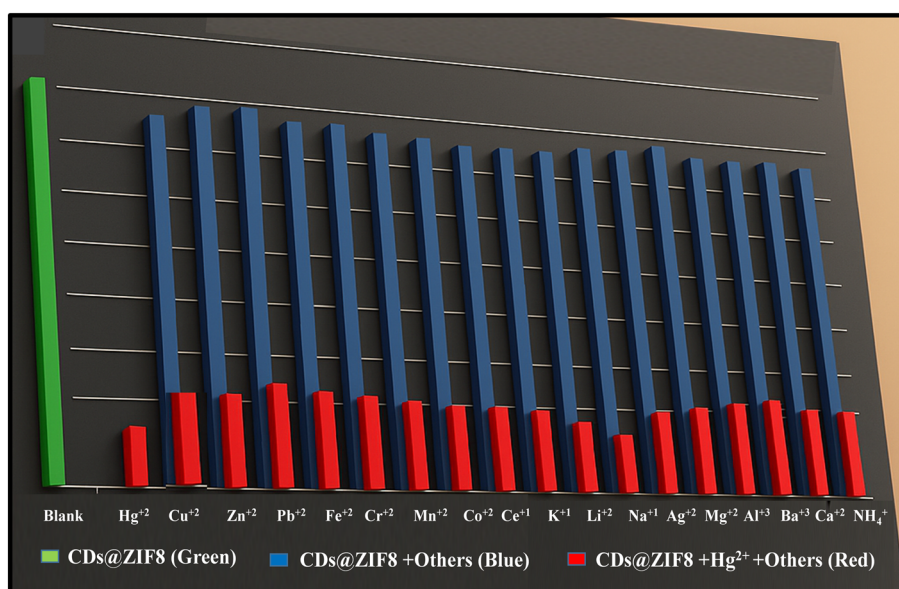

Fig. 7 Evaluation of the anti-interference capability of CDs@ZIF-8 toward Hg^{2+} detection in the presence of various competing metal ions, highlighting its high selectivity and stability.
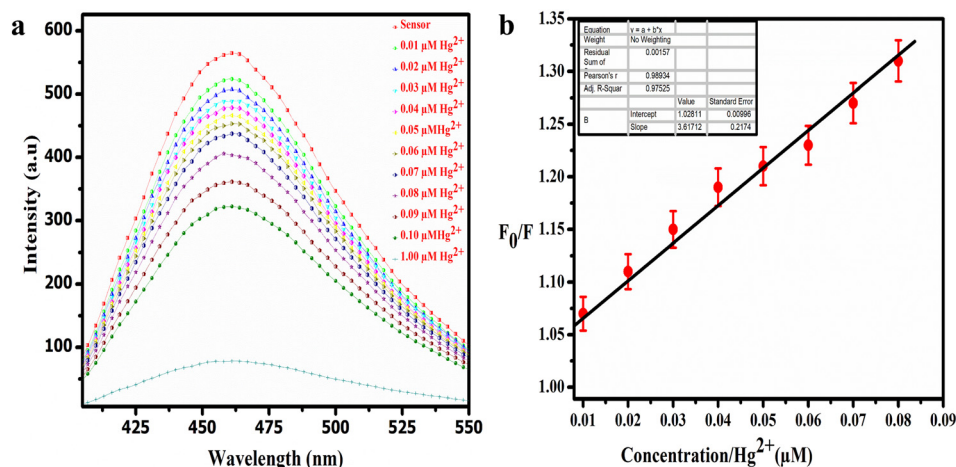
Fig. 8 (a) Fluorescence emission spectra of CDs@ZIF-8 with varying concentrations of Hg^{2+} ions. (b) Linear correlation between the relative fluorescence intensity (F_0/F) and Hg^{2+} concentration ranging from 0.01 to 1.00 μM, demonstrating quantitative sensing capability.

K_{sv} is the quenching constant. The quenching constant K_{sv} is calculated to be $6.27 \times 10^{-6}\,M^{-1}$, indicating a strong linear correlation with a coefficient of determination $R^2 = 0.989$. The linear relationship can be expressed by the equation: $y = 3.617\,[M] + 1.028$. The sensing system's detection limit (LOD) was determined using the formula $LOD = 3\sigma/K$, with a signal-to-noise ratio (S/N) of 5. The calculated LOD is 83 nM, which is significantly lower than the maximum Hg^{2+} concentration of 51 μM allowed in drinking water, as established by the U. S. Environmental Protection Agency (EPA).[52] The CDs@ZIF-8-based fluorescence sensing platform demonstrates remarkable potential for detecting Hg^{2+} in real water samples. Its strong resistance to external interference, broad linear detection range, and low detection limit outperform many other reported materials. A detailed comparison of CDs@ZIF-8 with other Hg^{2+} detection materials is presented in Table 1, highlighting its superior performance parameters.

3.4. Sensing mechanism

The fluorescence quenching of CDs@ZIF-8 upon Hg^{2+} addition is primarily governed by two synergistic processes: electron transfer and specific coordination interactions. The surface of CDs contains functional groups such as amino ($-NH_2$), hydroxyl ($-OH$), and carboxyl ($-COOH$), which exhibit a strong affinity toward Hg^{2+} ions. Upon binding, stable coordination complexes are formed, and Hg^{2+} ions act as efficient electron acceptors, enabling non-radiative electron transfer from the excited state of CDs to Hg^{2+}, thereby quenching the fluorescence signal.[60,61] Additionally, encapsulation of CDs within the porous ZIF-8 framework prevents aggregation, maintains high surface area, and preserves photoluminescence efficiency. The structural confinement of ZIF-8 also provides selective accessibility for Hg^{2+} ions while excluding larger or less interactive ions, thereby enhancing selectivity.[62,63] Beyond fluorescence quenching, the adsorption and accumulation effect between CDs@ZIF-8 and Hg^{2+} was investigated.[64] After CDs@ZIF-8 was added to the transparent Hg^{2+} solution (Fig. S9A), the solution turned milky with white precipitates (Fig. S9B), indicating strong binding and accumulation of Hg^{2+} ions. The enrichment effect not only improves detection sensitivity but also enhances selectivity. Moreover, upon introduction of Hg^{2+} ions, a significant enhancement and broadening of the adsorption spectrum is observed across the entire range, with a prominent increase in the visible region (400–600 nm) as

Table 1 Comparison of the sensitivity of other reported fluorescence detection methods of Hg^{2+} with our reported sensor

Materials	Detection method	Linear range (μM)	LOD	Ref.
Quantum dots	Fluorescence	0.2–2	1 μM	53
Tetraphenylethene (TPE)-modified rhodanine chemosensor	Fluorescence	0–30	0.6 μM	54
Gum-based AgNPs	Colorimetric	0–2000	0.5 mM	55
Coumarin-derived chemo sensor	Fluorescence	—	0.19 μM	56
Europium-doped CDs	Fluorescence	10–100	4–5 μM	57
Dielectric barrier discharge reactor	Atomic absorption spectrometry	1–100	100 μM	58
Eutectic solvent and chemical vapor generation	Inductively coupled plasma optical emission spectrometry	2.5–120	0.6 μM	59
Carbon dot-encapsulated metal organic framework	Fluorescence	0–1.0	83 nM	This work

shown in Fig. S10. This pronounced change in optical response can be attributed to the coordination of Hg^{2+} with the nitrogen and oxygen functionalities of CDs and ZIF-8 linkers, leading to altered electronic states and charge transfer transitions. Such evidence strongly supports the robust affinity of Hg^{2+} toward CDs@ZIF-8 and highlights its dual role in both fluorescence quenching and optical adsorption modulation, confirming its potential as an efficient platform for mercury detection.

3.5. Real water sample analysis

To evaluate the practical applicability of the sensor for real water sample analysis (river water, lake water, and tap water), fluorescence sensing experiments were conducted using the standard addition method. Three distinct concentrations of Hg^{2+} (0.03, 0.06, and 0.09 $\mu mol\ L^{-1}$) were spiked into each water sample, and fluorescence measurements were recorded with a fluorescence spectrophotometer. The sensor's detected Hg^{2+} concentrations closely matched the spiked values, as detailed in Table S2, with excellent recovery rates ranging from 96.54% to 99.01%. These findings demonstrate that the CDs@ZIF-8 sensor is highly effective for detecting Hg^{2+} in real water samples.

4. Conclusions

In summary, an innovative fluorescent sensor, CDs@ZIF-8, was successfully fabricated by encapsulating water-soluble, blue-emitting CDs within the porous framework of ZIF-8 using a facile one-pot synthesis strategy. This innovative sensor exhibited exceptional selectivity and sensitivity for detecting Hg^{2+} in aqueous environments, highlighting its significant potential for practical applications in environmental monitoring and water quality assessment. The CDs@ZIF-8 system exhibited excellent luminescence properties and maintained structural integrity within the MOF. Fluorescence quenching studies demonstrated that the sensor exhibits exceptional sensitivity toward mercury ions, detecting even trace levels within a broad linear range of 0–1.0 μM and a low LOD of 83 $nmol\ L^{-1}$. This high performance is attributed to the strong interaction between Hg^{2+} and the surface functional groups of the CDs, resulting in pronounced fluorescence quenching. We further validated the sensor's practicality by testing real environmental water samples, which confirmed its high sensitivity and selectivity in detecting trace amounts of Hg^{2+} under actual conditions. The material displayed good stability, repeatability, and minimal interference from other metal ions, demonstrating its reliability for environmental monitoring applications. This work highlights the potential of CDs@ZIF-8 for use as a mercury ion sensor, with real-world relevance for detecting toxic pollutants in natural water sources. Future studies could explore extending this approach to the detection of other hazardous substances. Moreover, the scalability and environmentally friendly synthesis of CDs@MOF systems present opportunities for the development of practical sensing devices for real-world applications.

Conflicts of interest

There are no conflicts to declare.

Data availability

Supplementary information is available. See DOI: https://doi.org/10.1039/D5CE00811E

Data will be made available on reasonable request.

Acknowledgements

References

1 Y.-S. Wu, A. I. Osman, M. Hosny, A. M. Elgarahy, A. S. Eltaweil, D. W. Rooney, Z. Chen, N. S. Rahim, M. Sekar and S. C. B. Gopinath, *ACS Omega*, 2024, **9**, 5100–5126.

2 R. Pant, N. Mathpal, R. Chauhan, A. Singh and A. Gupta, in *A Review of Mercury Contamination in Water and Its Impact on Public Health, Earth and Environmental Sciences Library (EESL)*, ed. N. Kumar, Springer, Cham, 2024, ch. 4, pp. 93–115.

3 M. G. Metwally, A. H. Benhawy, R. M. Khalifa, R. M. El Nashar and M. Trojanowicz, *Molecules*, 2021, **26**, 6515.

4 M. Mititelu, S. M. Neacşu, Ş. S. Busnatu, A. Scafa-Udrişte, O. Andronic, A.-E. Lăcraru, C.-B. Ioniţă-Mîndrican, D. Lupuliasa, C. Negrei and G. Olteanu, *Toxics*, 2025, **13**, 333.

5 A. Chamoli and S. K. Karn, in *A Review of Mercury Contamination in Water and Its Impact on Public Health, Earth and Environmental Sciences Library (EESL)*, ed. N. Kumar, Springer, Cham, 2024, ch. 5, pp. 117–135.

6 X. Zhang, F. Li, J. Chao, Z. Li, G. Zhang, L. Zhai, L. Hu, H. Jiao and Z. Wang, *Anal. Chim. Acta*, 2024, **1307**, 342622.

7 A. S. Anil, S. Alam and L. K. Thakur, *J. Food Compos. Anal.*, 2024, **129**, 106092.

8 J. A. Carter, C. A. Barber, M. M. Wolle and P. J. Gray, *Anal. Bioanal. Chem.*, 2025, 1–16.

9 Q. Yang, Y. Zhao, H. Yu, X. Xiong and K. Huang, *Appl. Spectrosc. Rev.*, 2024, **59**, 652–677.

10 J. W. Lim, T.-Y. Kim and M.-A. Woo, *J. Biosens. Bioelectron.*, 2021, **183**, 113228.

11 A. Salek Maghsoudi, S. Hassani, K. Mirnia and M. Abdollahi, *Int. J. Nanomed.*, 2021, 803–832.

12 B. Li, T. Suo, S. Xie, A. Xia, Y.-j. Ma, H. Huang, X. Zhang and Q. Hu, *TrAC, Trends Anal. Chem.*, 2021, **135**, 116163.

13 I. A. Lone and J. V. Rohit, *Inorg. Chem. Commun.*, 2025, 114918.

14 P. D. Modi, V. N. Mehta, V. S. Prajapati, S. Patel and J. V. Rohit, in *Carbon Dots in Analytical Chemistry: Detection and Imaging*, ed. S. K. Kailasa and C. M. Hussain, Elsevier, Amsterdam, 2022, ch. 2, pp. 15–29.

15 K. Sharma, A. Singh, R. Roopashree, J. Sharma, J. Gaur, S. Kumar and S. Kaushal, *ChemistrySelect*, 2025, **10**, e00774.

16 V. N. Mehta, J. B. Raval, S. K. Kailasa, J. V. Rohit and V. S. Prajapati, in *Functionalized Carbon Nanomaterials for Theranostic Applications*, ed. S. Mallakpour and C. M. Hussain, Micro and Nano Technologies, Elsevier, Amsterdam, 2023, ch. 3, pp. 55–74.

17 L. Ma, X. Long, Y. Ma and S. Wu, *Carbon Lett.*, 2024, **34**, 941–950.

18 S. Kumari, N. Sandhu, V. Saraswat and T. K. Sarkar, *Langmuir*, 2025, **41**, 12150–12165.

19 J. V. Rohit, V. N. Mehta, A. B. Patel, H. Tabasum and G. Spolia, in *Carbon Dots in Analytical Chemistry: Detection and Imaging*, ed. S. K. Kailasa and C. M. Hussain, Elsevier, Amsterdam, 2022, ch. 9, pp. 97–108.

20 S. Das, P. Somu, A. K. Yadav, P. K. Hopke and S. Paul, *Environ. Sci.: Nano*, 2024, **11**, 739–765.

21 K. Saczuk, M. Dudek, K. Matczyszyn and M. Deiana, *Nanoscale Horiz.*, 2024, **9**, 1390–1416.

22 Y. Ru, G. I. N. Waterhouse and S. Lu, *Aggregate*, 2022, **3**, e296.

23 H. Wang, L. Ai, H. Song, Z. Song, X. Yong, S. Qu and S. Lu, *Adv. Funct. Mater.*, 2023, **33**, 2303756.

24 X. R. Zhang, T. B. Song, T. L. He, Q. L. Ma, Z. F. Wu, Y. G. Wang and H. M. Xiong, *Adv. Funct. Mater.*, 2025, **35**, 2419219.

25 R. Kumari, M. Prajapati and C. Ravi Kant, *Adv. Sustainable Syst.*, 2024, **8**, 2400109.

26 F.-J. Chen and J. Yu, *Acc. Chem. Res.*, 2025, 1605–1608.

27 A. Kondinski, P. Rutkevych, L. Pascazio, D. N. Tran, F. Farazi, S. Ganguly and M. Kraft, *Digital Discovery*, 2024, **3**, 2070–2084.

28 W. Mandal, S. Fajal, A. V. Desai and S. K. Ghosh, *Coord. Chem. Rev.*, 2025, **524**, 216326.

29 V. Virender, V. Pandey, G. Singh, P. K. Sharma, P. Bhatia, A. A. Solovev and B. Mohan, *Top. Curr. Chem.*, 2024, **383**, 3.

30 X. Wei, J. Liu, H. Yan, T. Li, Y. Wang, Y. Zhao, G. Li and G. Zhang, *Sep. Purif. Technol.*, 2025, **353**, 128348.

31 P. Verma, Y. Kondo, Y. Kuwahara, T. Kamegawa, K. Mori, R. Raja and H. Yamashita, *Catal. Rev.*, 2021, **63**, 165–233.

32 Q.-Y. Yu, G.-Y. Zhai, T.-L. Cui, H. Su, Z.-H. Xue, J.-J. Zhang, P. J. Pauzauskie, S.-i. Hirano, X.-H. Li and J.-S. Chen, *Sci. China: Chem.*, 2019, **62**, 434–439.

33 W. Shi, W. Li, W. Nguyen, W. Chen, J. Wang and M. Chen, *Mater. Today Adv.*, 2022, **15**, 100273.

34 M.-Y. Li, J. Liu, R. Gao, D.-Y. Lin, F. Wang and J. Zhang, *Mater. Today Adv.*, 2021, **10**, 100145.

35 Y. Zhao, H. Zeng, X.-W. Zhu, W. Lu and D. Li, *Chem. Soc. Rev.*, 2021, **50**, 4484–4513.

36 V. Gargiulo, M. Alfè, L. Giordano and S. Lettieri, *Chem*, 2022, **10**, 290.

37 I. A. Lone and J. V. Rohit, *Inorg. Chim. Acta*, 2025, 122830.

38 C. Dai, Y. Zhao, P. Chen, J. Liu, C. Wang, L. Jiang, Y. Huang, M. Feng, R. Ouyang and Y. Miao, *Int. J. Electrochem. Sci.*, 2022, **17**, 220545.

39 Y. Hong, Y. Wang, Y. Guo, K. Wang, H. Wu, C. Zhang and Q. Zhang, *Z. Anorg. Allg. Chem.*, 2022, **648**, e202200115.

40 W.-H. Huang, X.-X. Zhang and Y.-N. Zhao, *Dalton Trans.*, 2021, **50**, 15–28.

41 X. Fu, H. Li, R. Lv, D. Hong, B. Yang, W. Gu and X. Liu, *J. Solid State Chem.*, 2018, **264**, 35–41.

42 J.-M. Yang, X.-W. Hu, Y.-X. Liu and W. Zhang, *Microporous Mesoporous Mater.*, 2019, **274**, 149–154.

43 E. Ploetz, H. Engelke, U. Lächelt and S. Wuttke, *Adv. Funct. Mater.*, 2020, **30**, 1909062.

44 X. Xie, M. Pan, L. Hong, K. Liu, J. Yang, S. Wang, Y. Song and S. Wang, *Sens. Actuators, B*, 2022, **368**, 132196.

45 X. Hu, Y. Guo, J. Zhang, X. Wang, G. Fang and S. Wang, *J. Chem. Eng.*, 2022, **433**, 134499.

46 S. R. Venna, J. B. Jasinski and M. A. Carreon, *J. Am. Chem. Soc.*, 2010, **132**, 18030–18033.

47 M. Pan, J. Sun, Y. Wang, J. Yang, Z. Wang, L. Li and S. Wang, *Food Chem.*, 2024, **442**, 138461.

48 Q. Tan, R. Zhang, G. Zhang, X. Liu, F. Qu and L. Lu, *Anal. Bioanal. Chem.*, 2020, **412**, 1317–1324.

49 M. Wang, Y. Chen, H. Luo, M. Wang, L. Li, Z. Xia, Y. Xu and Y. Huang, *Int. J. Biol. Macromol.*, 2025, **291**, 139985.

50 K. Yi and L. Zhang, *J. Hazard. Mater.*, 2020, **389**, 122141.

51 X. Guo, C. Liu, N. Li, S. Zhang and Z. Wang, *R. Soc. Open Sci.*, 2018, **5**, 171922.

52 G. M. Escandar and A. C. Olivieri, *ACS Omega*, 2022, **7**, 39574–39585.

53 B. Cao, C. Yuan, B. Liu, C. Jiang, G. Guan and M.-Y. Han, *Anal. Chim. Acta*, 2013, **786**, 146–152.

54 J.-j. Tian, D.-d. Deng, L. Wang, Z. Chen and S. Pu, *Front. Chem.*, 2022, **9**, 811294.

55 S. Y. Sharaf Zeebaree, O. I. Haji, A. Y. S. Zeebaree, D. A. Hussein and E. H. J. C. Hanna, *Catalysts*, 2022, **12**, 1464.

56 M. Gosi, A. C. Kumar and Y. Sunandamma, *J. Fluoresc.*, 2022, **32**, 2379–2393.

57 C. Correia, J. Martinho and E. Maçôas, *Nanomaterials*, 2022, **12**, 385.

58 G. d. S. C. Junior, D. L. G. Borges, M. Svoboda, J. Dědina and J. Kratzer, *Spectrochim. Acta, Part B*, 2023, **200**, 106596.

59 S. J. Abellán-Martín, J. Pérez, F. C. Pinheiro, J. A. Nóbrega, M. Á. Aguirre, L. Vidal and A. Canals, *Adv. Sample Prep.*, 2023, **7**, 100084.

60 H. Liu, H. Li, K. Du and H. Xu, *Mater. Today Commun.*, 2022, **33**, 104880.

61 D. Dai, C. Zhang, N. T. D. Thuy, G. Zhao, W. Lu and J. Fan, *Diamond Relat. Mater.*, 2022, **126**, 109076.

62 M. Li, Y. Duan, J. Wei, H. Lin, Q. Feng, Y. Tuo, Z. Chen, J. Lv, M. Li and Q. Wu, *J. Environ. Chem.*, 2022, **10**, 108852.

63 H.-Y. Xie, J.-G. Liang, Z.-L. Zhang, Y. Liu, Z.-K. He and D.-W. Pang, *Spectrochim. Acta, Part A*, 2004, **60**, 2527–2530.

64 H. Guo, X. Wang, N. Wu, M. Xu, M. Wang, L. Zhang and W. Yang, *Anal. Methods*, 2020, **12**, 4058–4063.